PAN

Opto-Electronics Review

journal homepage: https://journals.pan.pl/opelre

Fabrication and characterisation of the PiN Ge photodiode with poly-crystalline Si:P as n-type region

Quentin Durlin*, Abdelkader Aliane, Luc André, Hacile Kaya, Mélanie Le Cocq, Valérie Goudon, Claire Vialle, Marc Veillerot, Jean-Michel Hartmann

Univ. Grenoble Alpes, CEA-Leti, F-38000 Grenoble, France

Article info

Article history:
Received 26 Sep. 2022
Received in revised form 21 Nov. 2022
Accepted 19 Dec. 2022
Available on-line 24 Feb. 2023

Keywords:
Germanium (Ge); photodiode; short-wave infrared detector.

Abstract

Germanium (Ge) PiN photodetectors are fabricated and electro-optically characterised. Unintentionally and p-type doped Ge layers are grown in a reduced-pressure chemical vapour deposition tool on a 200 mm diameter, <001>-oriented, p-type silicon (Si) substrates. Thanks to two Ge growth temperatures and the use of short thermal cycling afterwards, threading dislocation densities down to 10^7 cm^{-2} are obtained. Instead of phosphorous (P) ion implantation in germanium, the authors use *in situ* phosphorous-doped poly-crystalline Si (poly-Si) in the n-type regions. Secondary ion mass spectrometry revealed that P was confined in poly-Si and did not diffuse in Ge layers beneath. Over a wide range of tested device geometries, production yield was dramatically increased, with almost no short circuits. At 30 °C and at −0.1 V bias, corresponding to the highest dynamic resistance, the median dark current of 10 µm diameter photodiodes is in the 5–20 nA range depending on the size of the n-type region. The dark current is limited by the Shockley-Read-Hall generation and the noise power spectral density of the current by the flicker noise contribution. A responsivity of 0.55 and 0.33 A/W at 1.31 and 1.55 µm, respectively, is demonstrated with a 1.8 µm thick absorption Ge layer and an optimized anti-reflection coating at 1.55 µm. These results pave the way for a cost-effective technology based on group-IV semiconductors.

1. Introduction

Detection in the short-wave infrared (SWIR) domain is switching today from a niche market, principally dedicated to defence applications, to a global demand for consumer applications [1]. SWIR detectors development is mainly driven by light imaging detection and ranging (LIDAR) for use in autonomous vehicles. Although LIDAR exists in the visible and near-infrared [2], low-cost systems operating in the eye-safety region (wavelengths above 1.4 µm) are still under development due to the lack of an affordable area detector. Another emerging application is the integration of SWIR depth sensing and imaging modules in consumer devices for facial recognition and virtual reality [1].

Among competing non-cryogenic technologies, InGaAs/InP photodetectors are more mature and exhibit low dark current and high responsivity [3, 4]. For improving scalability, epitaxy of InGaAs on a large Si substrate has been demonstrated [5], but the dark current is much higher than on small (< 4 inches) InP substrates. This technology also requires costly heterogeneous integration where the detection circuit is reported on a complementary metal-oxide-semiconductor (CMOS) read-out integrated circuit (ROIC) using indium bumps. An alternative approach is the dies-to-wafer bonding using Cu-Cu hybridisation that has recently been demonstrated down to a 5 µm pitch [6]. Having recently emerged as a competitive technology, colloidal quantum dots (CQD) detectors are cheap, highly scalable, and with a pixel pitch as low as 1.6 µm [7–10]. Absorption peak of CQD can be tuned from

*Corresponding author at: quentin.durlin@cea.fr

https://doi.org/10.24425/opelre.2023.144550
1896-3757/ Association of Polish Electrical Engineers (SEP) and Polish Academic of Sciences (PAS). Published by PAS

visible to 2.1 µm [11], though its maximum absorption is lower than for bulk materials. The third technology is based on Ge, where recent technological progresses have been made. Detectors for diverse applications have been fabricated, such as: waveguides photodiodes [12–14] and avalanche photodiodes (APD) [15–18] for use in photonic integrated circuits (PIC), single-photon avalanche detectors (SPAD) [19–21] for direct time-of-flight (ToF) measurements, and current-assisted photonic demodulators (CAPD) for indirect ToF [22]. Despite many single photodetector fabrications, focal plane arrays (FPA) based on Ge are still scarce [22, 23], which is a clear sign of the low maturity of the fabrication process.

The lowest dark currents, in the 10^{-4}–10^{-3} A/cm^2 range, have been obtained in single photodiodes built on Ge bulk [24, 25]. However, fabrication on Ge wafers [24] or on Ge-On-Insulator (GeOI) substrates [25, 26] limits the scalability of such integration. The key advantage of Ge is its full compatibility with the standard microelectronic process. Ge thick layers are grown either full sheet or locally in openings through oxide hard masks on Si wafers, due to a reduced pressure-chemical vapour deposition (RP-CVD). Ge can be deposited on 200 mm diameter silicon wafers [15, 27] and 300 mm diameter Si wafers [28] allowing high production yields. In order to accommodate the 4.2% lattice mismatch between the Ge layer and the Si substrate, a specific epitaxial growth technique has been developed. A two-step Ge growth process, first at 400 °C then at 750 °C, followed by a short-duration thermal cycling between 750 °C and 875 °C, was shown to yield threading dislocation densities close to 10^7 cm^{-2} [29]. Because of the difference between the coefficients of thermal expansion of Ge and Si and the temperature at which epitaxial growth and thermal cycling occur (in-between 750 and 875 °C), Ge has a residual tensile strain around +0.15% [27]. Tensile strain narrows the bandgap of Ge, extending its cut-off wavelength to values above 1600 nm. At 1550 nm, Ge epitaxial layer has then an appreciable absorption coefficient of around 4000 cm^{-1} [27], making this material highly attractive for silicon photonics or applications where eye-safety is of primary concern such as LIDAR.

Fabrication of FPAs of Ge photodiodes requires the dark current reduction. Efforts are focused on different stages of the fabrication process. For instance, Takenaka *et al.* successfully demonstrated the dark current reduction using GeO_2 passivation of Ge bulk photodiodes [24]. However, integration of Ge oxide in a large-scale fabrication process is still a challenge because of its solubility in water or its desorption at low temperature (< 420 °C) [30]. Another strategy is to integrate a larger bandgap material on top of the Ge surface like a Si capping layer [29, 31].

P ion implantation is typically used for the n-type doping of Ge. Rapid thermal annealing (RTA) yields a full recrystallisation of the damaged area and dopants activation. However, high diffusion coefficient of P in Ge requires a low thermal budget fabrication process. Laser thermal annealing (LTA) yields higher activation of dopants [32] and is useful for realisation of abrupt N^+-P junctions. The feasibility of gas-phase doping with arsenide (As) that has the advantage of not damaging the crystal, leading to a very low dark current [24] should also be noted. However, its scalability is poor.

At CEA-Leti, the authors have already improved the epitaxial growth of Ge on Si and the passivation of photodetectors [27]. In this work, the authors propose to change the n-type region of the PiN photodiode for a better scalability of their fabrication process. The n-type region of their Ge photodetector is made of *in situ* P-doped polycrystalline silicon (poly-Si:P). First, the authors detail the fabrication process of the photodetector and the properties of the poly-Si:P layer. Finally, electrical and optical characterisations of the photodetectors are discussed.

2. Fabrication process

Devices were fabricated on a 200 mm diameter, <100>-oriented, Si substrates with a p-type doping of 10^{15} cm^{-3}. Ge layers were grown thanks to GeH_4 in an AMAT Epi-Centura 5200 RP-CVD reactor. At first, an intrinsic 50 nm thick Ge buffer layer was grown at 400 °C, 100 Torr. Misfit dislocations due to the lattice mismatch between Ge and Si were confined in this buffer layer. Then, a 200 nm thick Ge layer *in situ* boron-doped with a concentration of a few 10^{19} cm^{-3} forming the P^+ layer of the PiN photodiode was epitaxed at the same temperature and pressure (thanks to GeH_4 and B_2H_6). Then, an unintentionally doped (UID) 1.5 µm thick Ge layer forming the absorption region of the PiN photodiode was deposited at 750 °C, 20 Torr. The top of the 1.5 µm thick Ge surface was capped with a 15 nm thick Ge(3 nm)/$Si_{0.7}Ge_{0.3}$(3 nm) stack in order to passivate the Ge layer. A thermal cycling under H_2 between 750 °C and 875 °C was used, prior to the Ge capping, in order to reduce the threading dislocations density (TDD) to a value close to 10^7 cm^{-2}.

The n-type region, made of poly-Si layer *in situ* P-doped with a $1.5 \cdot 10^{20}$ at/cm^{-3} concentration, was deposited in openings through a 100 nm thick TEOS (tetraethyl orthosilicate) hard mask – the "TEOS" is a low density SiO_2, compared with thermal oxide, deposited by plasma-enhanced chemical vapour deposition (PECVD) technique at 400 °C using TEOS precursor. A low-pressure chemical vapour deposition (LPCVD) furnace was used for the poly-Si:P deposition at 580 °C (with SiH_4 and PH_3 as precursors). After deposition, excess poly-Si:P was removed by chemical mechanical polishing (CMP). N-type regions have diameters varying from two to hundreds of micrometres. Figure 1(a) shows a scanning electron microscope (SEM) image of the structure after planarization, with a poly-Si:P n-type region with a 5 µm diameter.

Devices were isolated by etching the Ge layer until the Ge:B layer was reached. Then, the intrinsic Ge layer was passivated using TEOS deposition. The process flow ended with metallization: Ni(10 nm)/TiN(10 nm) stacks were deposited to fabricate electrical contacts. The first thermal annealing, at 300 °C during 30 s under N_2 atmosphere, yielded the highly resistive Ni_2Si phase. Then, selective wet etching removed TiN and part of the Ni that did not react with Si. At last, the second thermal annealing, at 450 °C during 30 s in N_2 yielded the low resistive NiSi silicide phase. Figure 1(b) is a cross-section view of the Ge photodiode showing dimensions D (diameter of the diode) and φ (diameter of the n-type region).

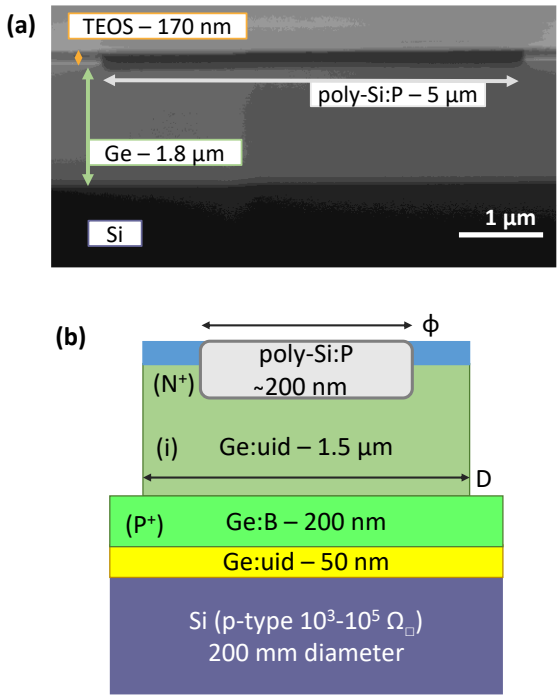

Fig. 1. A cross-sectionnal SEM image of the Ge photodiode after deposition and CMP of the poly-Si:P n-type region (a); A schematic of the Ge photodiode showing its diameter (D) and its n-type region diameter (φ) (b).

3. N-type region layer characterisation

At the end of the fabrication process, strain and composition of the deposited poly-Si:P layer were characterised. Strain was measured by the Raman spectroscopy and results are displayed in Fig. 2. Optical excitation of the sample was performed with a 532 nm laser at a power of 0.1 mW. The Lorentzian fit of the data gives a peak located at 520.77 cm^{-1} and a full width at half maximum (FWHM) of 6.34 cm^{-1}. For a fully relaxed poly-Si, the peak position is at 521 cm^{-1} [33] and the Raman shift is therefore $\Delta\omega = -0.23$ cm^{-1}. This corresponds to a biaxial tensile strain of $\varepsilon_{//} = -\Delta\omega/b^{Si\text{-}Si} < 0.05\%$ with $b^{Si\text{-}Si} = 815$ cm^{-1} [34]. Strain in the n-type poly-Si:P region is thus negligible.

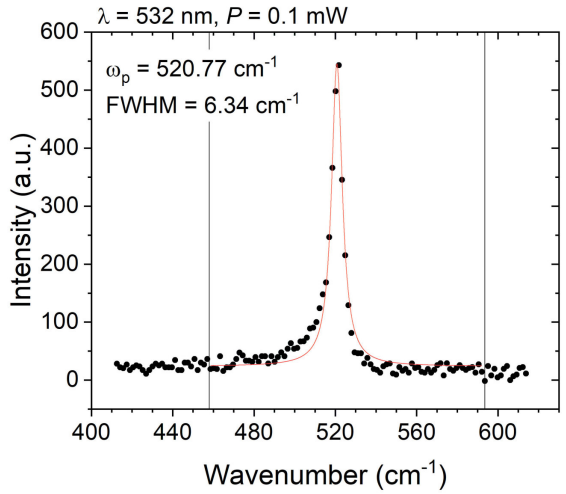

Fig. 2. Raman spectrum of the n-type poly-Si:P layer deposited by LPCVD on Ge. Data are fitted with a Lorentzian peak.

Secondary ion mass spectrometry (SIMS) profiled the P concentration in the thickness of the deposited poly-Si:P layer. Measurement was carried out on a large 100×100 μm^2 n-type region. Results are shown in Fig. 3. The main regions of the structure are identified when looking at the ^{18}O, ^{28}Si, and ^{72}Ge raw profiles (in counts/s): TEOS passivation layer on top of the wafer until a depth of 420 nm, poly-Si:P n-type region between 420 nm and 650 nm, and Ge epitaxial layer below. The Ge profile gradually increases in the poly-Si layer, which might be a sign of Ge diffusion during the deposition of the poly-Si:P on top of it. The Ge peak at 500 nm indicates that metallization occurred on a SiGe alloy. At the interface between Si and Ge, the origin of the O peak is less clear: it probably reveals an actual oxidation of the poly-Si:P surface but a contribution coming from a change in the ionization yield of ^{18}O – between Si and Ge – cannot be excluded. Regarding the ^{31}P concentration profile, it is of maximum accuracy in the Si layer where the quantification factor of P is perfectly known; in the poly-Si layer with diffused Ge species, the order of magnitude can be considered as respected, but the quantification is not reliable. The P concentration is of $2–3 \cdot 10^{20}$ at/cm^3 in poly-Si, close to the expected value of $1.5 \cdot 10^{20}$ at/cm^3. It then drops in Ge showing that P is confined in the poly-Si:P deposited layer and does not diffuse in the layer below.

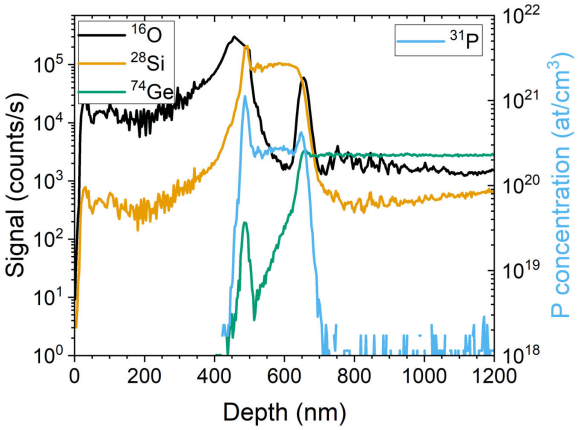

Fig. 3. SIMS depth profiles of ^{18}O, ^{28}Si and ^{74}Ge in counts/s, and ^{31}P depth profile in at/cm^3.

4. Electro-optical characterisation

Devices with a diameter $D = 10$ µm were characterised on an automatic prober at 30 °C in the dark. From 68 tested devices with $\varphi = 4$ µm, first quartile, median, and third quartile of dark current at −0.1 V are 5.8, 8.7, and 18.4 nA, respectively. There was no short circuit. Fabrication process with poly-Si:P layer as n-type region results in high yield with a low dispersion on dark current. In the following, the authors focus on representative single detectors (with measured dark current close to the median current).

4.1 Dark current characterisation

Dark current-voltage characteristics at different temperatures are summarised in Fig. 4 for a device with a diameter $D = 10$ µm and an n-type region with a diameter of $\varphi = 4$ µm. As the temperature increases from 25 to

90 °C, the maximum of the dynamic resistance R_d shifts from −0.1 to −0.2 V. At 30 °C and −0.1 V, R_d is $3.0 \cdot 10^7$ Ω and dark current $7.8 \cdot 10^{-9}$ A, which corresponds to a dark current density of $1 \cdot 10^{-2}$ A/cm^2. For comparison, two dark current densities at the same bias and at room temperature are reported: 1) Oehme *et al.* measured $1 \cdot 10^{-3}$ A/cm^2 on a 3 µm^2 area detector but with only a 300 nm thick Ge absorption layer [23]; 2) Rouse *et al.* obtained a current density as low as $6 \cdot 10^{-6}$ A/cm^2 for a 100×100 µm^2 device [28]. The dark current dependence with temperature was studied by calculating the activation energy E_a (in eV) using the following formula:

$$I(A) = I_0 * \exp\left(-\frac{E_a}{k_B T}\right), \quad (1)$$

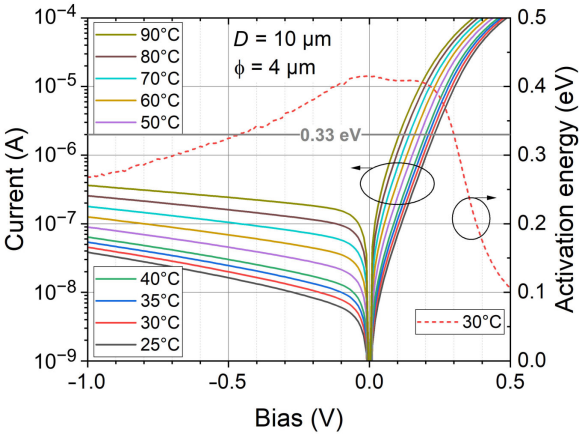

Fig. 4. *I-V* caracteristics under dark conditions at different temperatures for a device with $D = 10$ µm and a diameter of $\varphi = 4$ µm for n-type region. Activation energy at 30 °C as a function of bias is also reported.

where k_B is the Boltzmann constant, T is the temperature and I_0 is the factor in ampere (that varies slightly with the temperature compared to the exponential term). Activation energy at 30 °C, calculated from the current at 25 and 35 °C, is plotted as a function of voltage in Fig. 4. At −0.1 V, an activation energy of 0.40 eV is measured. This value is close to 0.33 eV, e.g., half the 0.66 eV indirect bandgap of Ge: it indicates that the main contribution to the dark current is the SRH (Shockley-Read-Hall) generation mechanism. As the reverse bias increases, the activation energy decreases from 0.40 to less than 0.33 eV at −0.5 V: such a drop of E_a below mid-bandgap was interpreted in Ge diodes as a contribution from a trap-assisted-tunnelling current [35, 36]. In forward bias, ideality factor is calculated from a linear fit of the natural logarithm of the dark current on the range 3–8 in qV/kT units. Ideality factor decreases from 1.46 to 1.40 as temperature increases from 25 to 50 °C. At higher temperatures, series resistances prevent precise extraction of the ideality factor. Ideality factor between 1 and 2 suggests a mix of diffusion and SRH current in forward bias.

The dependence of the dark current with a diameter of the poly-Si:P n-type region was also studied. The Arrhenius plots at −0.1 V are shown in Fig. 5 for $D = 10$ µm and φ ranging from 2 to 7 µm. Activation energy was fitted from the natural logarithm of the current over two-temperature sets: low temperature between 25 and 40 °C, and high temperature between 70 and 90 °C. E_a did not depend on the n-type region diameter φ. The linear increase of the median dark current with the area of the n-type region suggests that the main contribution to the dark current is the SRH generation in the space charge region (SCR) at room temperature. The increase of E_a from 0.40 to 0.51 eV with temperature indicates the increasing diffusion current contribution.

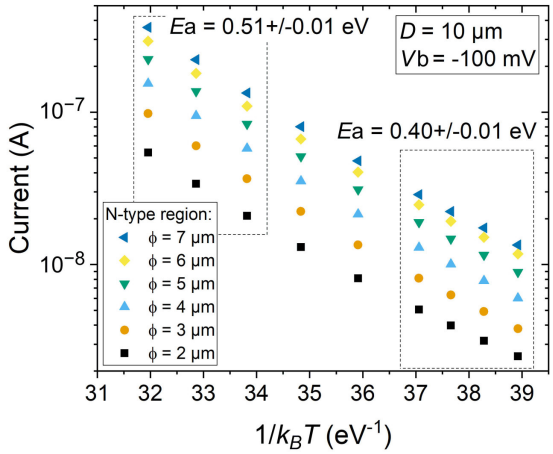

Fig. 5. Arrhenius plots of the dark current at −0.1 V for devices with different diameters φ of the poly-Si:P n-type region.

4.2 *Noise characterisation*

Noise at 30 °C and under dark conditions was measured on devices with 10 µm diameters. Reference bias was set on the bottom p-type region and a varying potential applied on the n-type region through a low-noise pre-amplifier. A dynamic signal analyser (Agilent 35670A) measured current fluctuations of the device under test and performed the fast-Fourier transformation (FFT) of the signal.

In a reversed bias photodiode, noise is the resultant of different contributions. Johnson noise originates from random thermal motion of charge carriers in resistive materials. Shot noise comes from a discrete nature of electrical charges. Both are white noises and intrinsic to electronic devices. The flicker noise has an intensity that is inversely proportional to the frequency. Its origin, still under debate, comes from fluctuations of the density or mobility of carriers. Squared total noise current σ_{total}^2 in A^2/Hz is given by [37]

$$\begin{aligned}\sigma_{total}^2 &= \sigma_{Johnson}^2 + \sigma_{shot}^2 + \sigma_{flicker}^2 \\ &= \frac{4k_B T}{R_d} + 2qI_{dark} + s_0 \frac{I_{dark}^{\beta}}{f^{\gamma}}, \end{aligned} \quad (2)$$

where q is the electric charge, k_B the Blotzmann constant, T is the temperature in K. I_{dark} and R_d are the dark current and the dynamic resistance at the operation bias. In a flicker noise empirical expression, f is the frequency in Hz, β and γ are the fitting parameters that are usually close to 2 and 1, respectively and s_0 is the unit less factor.

Noise measurements at different bias in Fig. 6 are from the photodiode with a diameter $D = 10$ µm and a diameter of $\varphi = 4$ µm for the poly-Si:P n-type region. Johnson and Schottky contributions are negligible compared to the measured noise. Fitting the data with $1/f$ expression in the 1–30 Hz range gives a γ parameter equal to 1±0.1 for bias between −0.02 and −0.5 V. Similar results are obtained on

diodes by the varying parameter φ. Figure 7 shows current dependence of squared noise current at 10 Hz for different photodiode geometries. The parameter β in the flicker noise expression is obtained by data fitting.

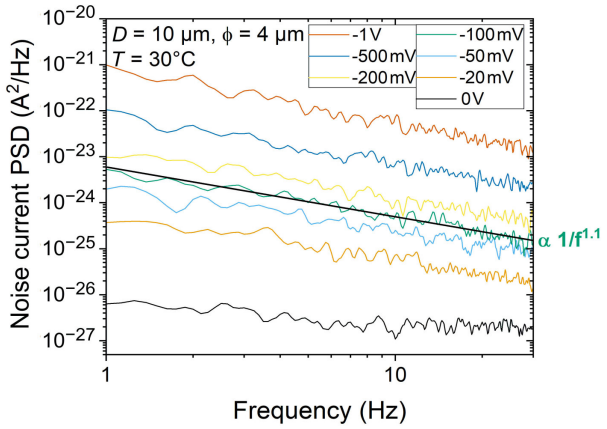

Fig. 6. Noise power spectral density (PSD) of current at different reverse bias on a $D = 10$ µm diameter photodiode with a $\varphi = 4$ µm-diameter n-type region.

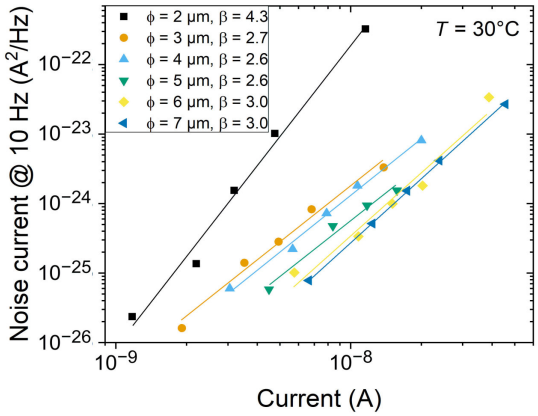

Fig. 7. Noise current at 10 Hz as a function of the current. Each curve results from measurements on $D = 10$ µmdiameter photodiodes with different diameters φ of the poly-Si:P n-type region.

Values of β greater than 2 may indicate additional noise sources such as contact resistance or tunnelling current. To support this idea, the authors compare β values with the activation energy calculated at −0.5 V and 30 °C (as calculated in Fig. 4). For lower β values of 2.6–2.7 (photodiodes with $\varphi = 3$, 4, 5 µm), the activation energy is around 0.325 eV; for intermediate β values of 3.0 (photodiodes with $\varphi = 6$, 7 µm), the activation energy is around 0.305 eV; for high β value of 4.3 (photodiodes with $\varphi = 2$ µm), activation energy is around 0.240 eV. The value of β scales inversely with activation energy; further analysis should be done to confirm this trend.

The temperature dependence of the noise current in A/Hz$^{0.5}$ at 10 Hz and −0.1 V was investigated in Fig. 8. Dark current dependence reported in Fig. 5 for the same device is also reproduced for comparison. Activation energy for noise current is 0.33 eV, e.g., half the Ge bandgap. This indicates that the spatial origin of the noise current is the SCR of the photodiode. Measurements of noise current with temperature on devices with the varying φ gave similar E_a close to half the bandgap.

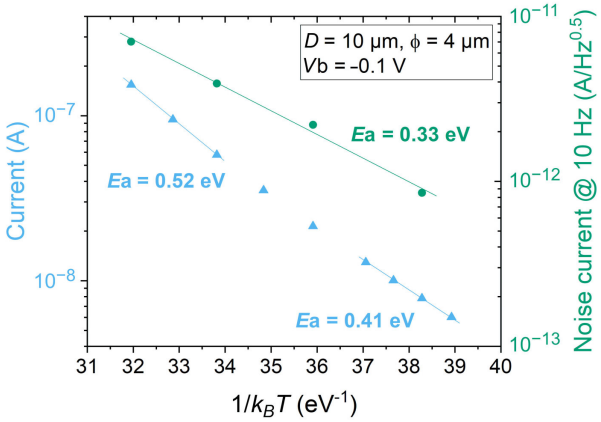

Fig. 8. Arrhenius plots of the dark current at −0.1 V and noise current at 10 Hz for a device with $D = 10$ µm and $\varphi = 4$ µm.

4.3 *Responsivity characterisation*

Responsivity of the Ge photodiode was measured at a temperature of 25 °C. Two lasers, at 1.31 and 1.55 µm (Yenista Optics), with adapted attenuators were used for illumination with an optical power varying from 10^{-2} to 10^{1} µW. Light was injected thanks to a single-mode optical fibre with a tip located at a distance of 20 µm above the surface of the wafer and a 10.5° incidence angle. The diameter of the optical spot was around 20 µm. The authors thus used a device with a larger area ($D = 40$ µm diameter) to fully collect the incident light. Currents in dark conditions and under illumination at $\lambda = 1310$ nm are plotted in Fig. 9(a). There is almost no bias dependence of the photocurrent with bias. The photocurrent at −0.1 V bias is plotted as a function of optical power in Fig. 9(b): responsivity is 0.55 A/W [or 52% quantum efficiency (QE)] at 1.31 µm, and 0.33 A/W (or 26% QE) at 1.55 µm. It should be noted that devices are illuminated through a 250 nm thick TEOS anti-reflection coating in order to minimize reflection at 1.5 µm.

5. Conclusions

A Ge photodiode with an *in situ* P-doped poly-Si layer as an n-type contact region is evaluated. SIMS measurements indicate that P does not diffuse in the Ge layer underneath: the junction is thus abrupt. Almost all tested devices with a diameter $D = 10$ µm exhibit diode-like current-voltage characteristics. The dark current scales with the diameter of the n-type region φ, indicating that it originates from the space charge region. For a device with $\varphi = 4$ µm, the dark current density is about 1.0×10^{-2} A/cm^2 at 30 °C and at −0.1 V bias (corresponding to the maximum of the dynamic resistance). In the same operating conditions, an activation energy of 0.40 eV, close to half the Ge bandgap, is measured, indicating that the dark current is dominated by the SRH generation. Measure-ments of power spectral density of the noise current show the dominance of the flicker noise contribution. Its activation energy at −0.1 V is 0.33 eV. The spatial origin of the noise is thus also in the SCR. The responsivity is evaluated on a larger device at 0.55 and 0.33 A/W at 1.31 and 1.55 µm, respectively. These encouraging results are a steppingstone towards the fabrication of the Ge-based FPAs.

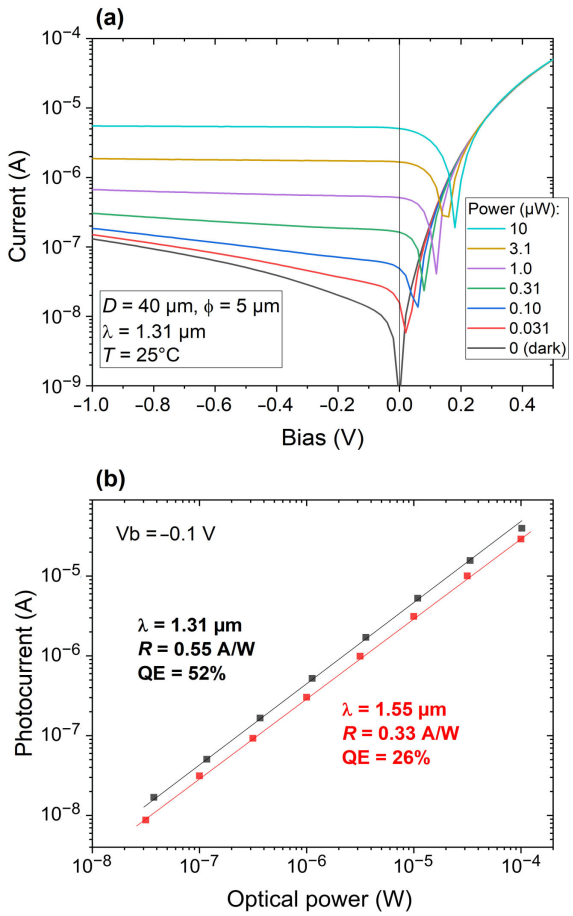

Fig. 9. *I-V* characteristics under illumination at various optical powers (a). Photocurrent at −0.1 V as a function of optical power for illumination at 1.31 and 1.55 μm (b).

Authors' statement

Design of photodiodes, A.A. and Q.D.; mask conception, A.A., V.G., and M.L.; semiconductor epitaxy, J.-M.H.; fabrication of devices, H.K. and M.L.; collection of data, C.V., M.V., A.A., and Q.D.; data analysis and interpretation, A.A. L.A., M.V., and Q.D.; writing the article, Q.D.; critical revision of the article, A.A.; final approval of article, L.A. and J.-M.H.

Acknowledgements

The authors are grateful for the financial support provided by the department of photonics and optics of CEA-Leti. Authors want to thank: Mehrez, Z., Vizzini, M., Vermandé, E., D'Alonzo, G., Ravix, S., Porzier, C., Brunet-Manquat, F., Laurent, R., Cammarata, C., Perrin, F., Despois, D., Beluffi, C., Dominguez, S., Lima, G., Benevent V. & Kerdiles, S. for their contribution to device fabrication; Grosse, P. for his help during responsivity measurements.

References

[1] Mounier, E. & Clouet, A. SWIR Imaging 2022: Technology and Market Trends Report. *Yole Group* (2022). https://www.yolegroup.com/product/report/swir-imaging-2022/

[2] Li, Y. & Ibanez-Guzman, J. LIDAR for autonomous driving: the principles, challenges, and trends for automotive lidar and perception systems. *IEEE Signal Proc. Mag.* **37**, 50–61 (2020). https://doi.org/10.1109/MSP.2020.2973615

[3] Yuan, H. *et al.* Low dark current small pixel large format InGaAs 2D photodetector array development at Teledyne Judson Technologies. *Proc. SPIE* **8353**, 835309 (2012). https://doi.org/10.1117/12.921232

[4] Nedelcu, A. *et al.* III-V detector technologies at Sofradir: Dealing with image quality. *Infrared Phys. Technol.* **94**, 273–279 (2018). https://doi.org/10.1016/j.infrared.2018.09.027

[5] Song, B., Shi, B., Tommaso Šuran-Brunelli, S., Zhu, S. & Klamkin, J. Low dark current and high speed InGaAs photodiode on CMOS-compatible silicon by heteroepitaxy. *IEEE J .Sel. Top. Quantum Electron.* **28**, 1–8 (2022). https://doi.org/10.1109/JSTQE.2021.3123052

[6] Manda, S. *et al.* High-definition Visible-SWIR InGaAs Image Sensor Using Cu-Cu Bonding of III-V to Silicon Wafer. in *2019 IEEE International Electron Devices Meeting (IEDM)* 16.7.1–16.7.4 (2019). https:/doi.org/10.1109/IEDM19573.2019.8993432

[7] Klem, E. J. D., Gregory, C., Temple, D. & Lewis, J. PbS colloidal quantum dot photodiodes for low-cost SWIR sensing. *Proc. SPIE* **9451**, 945104 (2015). https://doi.org/10.1117/12.2178532

[8] Georgitzikis, E. *et al.* Integration of PbS quantum dot photodiodes on silicon for NIR imaging. *IEEE Sensors J.* **20**, 6841–6848 (2020). https://doi.org/10.1109/JSEN.2019.2933741

[9] Gréboval, C. *et al.* Photoconductive focal plane array based on HgTe quantum dots for fast and cost-effective short-wave infrared imaging. *Nanoscale* **14**, 9359–9368 (2022). https://doi.org/10.1039/D2NR01313D

[10] Steckel, J. S., Pattantyus-Abraham, A. G., Josse, E., Mazaleyrat, E. & Rochereau, K. 66-1: High Resolution Quantum Dot Global Shutter Imagers. in *International Conference on Display Technology 2022 – SID Symposium Digest of Technical Papers* **52**, 975–977 (2021). https://doi.org/10.1002/sdtp.14852

[11] Gregory, C., Hilton, A., Violette, K. & Klem, E. J. D. 66-3: Invited paper: Colloidal quantum dot photodetectors for large format NIR, SWIR, and eSWIR imaging arrays. *SID Symposium Digest of Technical Papers* **52**, 982–986 (2021). https://doi.org/10.1002/sdtp.14854

[12] Feng, N.-N. *et al.* Vertical p-i-n germanium photodetector with high external responsivity integrated with large core Si waveguides. *Opt. Express.* **18**, 96–101 (2010). https://doi.org/10.1364/OE.18.000096

[13] Liow, T.-Y. *et al.* silicon modulators and germanium photodetectors on SOI: monolithic integration, compatibility, and performance optimization. *IEEE J. Sel. Top. Quantum Electron.* **16**, 307–315 (2010). https://doi.org/10.1109/JSTQE.2009.2028657

[14] Chen, L., Dong, P. & Lipson, M. High performance germanium photodetectors integrated on submicron silicon waveguides by low temperature wafer bonding. *Opt. Express* **16**, 11513–11518 (2008). https://doi.org/10.1364/OE.16.011513

[15] Virot, L. *et al.* Germanium avalanche receiver for low power interconnects. *Nat. Commun.* **5**, 4957 (2014). https://doi.org/10.1038/ncomms5957

[16] Huang, M. *et al.* Germanium on silicon avalanche photodiode. *IEEE J. Sel. Top. Quantum Electron.* **24**, 1–11 (2018). https://doi.org/10.1109/JSTQE.2017.2749958

[17] Kang, Y. *et al.* Monolithic germanium/silicon avalanche photodiodes with 340 GHz gain–bandwidth product. *Nat. Photonics* **3**, 59–63 (2009). https://doi.org/10.1038/nphoton.2008.247

[18] Wanitzek, M., Oehme, M., Schwarz, D., Guguieva, K. & Schulze, J. Ge-on-Si Avalanche Photodiodes for LIDAR Applications. in *2020 43rd International Convention on Information, Communication and Electronic Technology (MIPRO)* 8–12 (2020). https://doi.org/10.23919/MIPRO48935.2020.9245425

[19] Ke, S. *et al.* Design of wafer-bonded structures for near room temperature Geiger-mode operation of germanium on silicon single-photon avalanche photodiode. *Appl. Opt.* **56**, 4646–4653 (2017). https://doi.org/10.1364/AO.56.004646

[20] Vines, P. *et al.* High performance planar germanium-on-silicon single-photon avalanche diode detectors. *Nat. Commun.* **10**, 1086 (2019). https://doi.org/10.1038/s41467-019-08830-w

[21] Warburton, R. E. *et al.* Ge-on-Si single-photon avalanche diode detectors: design, modeling, fabrication, and characterization at wavelengths 1310 and 1550 nm. *IEEE Trans. Electron Devices* **60**, 3807–3813 (2013). https://doi.org/10.1109/TED.2013.2282712

[22] Chen, C.-L. *et al.* An Up-to-1400nm 500MHz Demodulated Time-of-Flight Image Sensor on a Ge-on-Si Platform. in *2020 IEEE*

International Solid-State Circuits Conference (ISSCC) 98–100 (2020). https://doi.org/10.1109/ISSCC19947.2020.9063107

[23] Oehme, M. *et al.* Backside illuminated "Ge-on-Si" NIR camera. *IEEE Sensors J.* **21**, 18696–18705 (2021). https://doi.org/10.1109/JSEN.2021.3091203

[24] Takenaka, M., Morii, K., Sugiyama, M., Nakano, Y. & Takagi, S. Dark current reduction of Ge photodetector by GeO_2 surface passivation and gas-phase doping. *Opt. Express* **20**, 8718 (2012). https://doi.org/10.1364/OE.20.008718

[25] Zhao, X. *et al.* High performance p-i-n photodetectors on Ge-on-insulator platform. *Nanomaterials* **11**, 1125 (2021). https://doi.org/10.3390/nano11051125

[26] Akatsu, T. *et al.* Germanium-on-insulator (GeOI) substrates—A novel engineered substrate for future high performance devices. *Mater. Sci. Semicond. Process.* **9**, 444–448 (2006). https://doi.org/10.1016/j.mssp.2006.08.077

[27] Aliane, A. *et al.* Fabrication and characterization of sensitive vertical P-i-N germanium photodiodes as infrared detectors. *Semicond. Sci. Technol.* **35**, 035013 (2020). https://doi.org/10.1088/1361-6641/ab6bf7

[28] Rouse, C. *et al.* Development of low dark current sige near-infrared PIN photodetectors on 300 mm silicon wafers. *Opt. Photon J.* **6**, 61–68 (2016). https://doi.org/10.4236/opj.2016.65009

[29] Hartmann, J. M. *et al.* Impact of the H_2 anneal on the structural and optical properties of thin and thick Ge layers on Si; Low temperature surface passivation of Ge by Si. *J. Cryst. Growth* **312**, 532–541 (2010). https://doi.org/10.1016/j.jcrysgro.2009.11.056

[30] Prabhakaran, K., Maeda, F., Watanabe, Y. & Ogino, T. Thermal decomposition pathway of Ge and Si oxides: observation of a distinct difference. *Thin Solid Films* **369**, 289–292 (2000). https://doi.org/10.1016/S0040-6090(00)00881-6

[31] Dong, Y. *et al.* Suppression of dark current in germanium-tin on silicon p-i-n photodiode by a silicon surface passivation technique. *Opt. Express* **23**, 18611–18619 (2015). https://doi.org/10.1364/OE.23.018611

[32] Shayesteh, M. *et al.* Optimized laser thermal annealing on germanium for high dopant activation and low leakage current. *IEEE Trans. Electron Devices* **61**, 4047–4055 (2014). https://hal.science/hal-01921394/document

[33] Firat, M. *et al.* In situ phosphorus-doped polycrystalline silicon films by low pressure chemical vapor deposition for contact passivation of silicon solar cells. *Sol. Energy* **231**, 78–87 (2022). https://doi.org/10.1016/j.solener.2021.11.045

[34] Rouchon, D., Mermoux, M., Bertin, F. & Hartmann, J.M. Germanium content and strain in $Si_{1-x}Ge_x$ alloys characterized by Raman spectroscopy. *J. Cryst. Growth* **392**, 66–73 (2014). https://doi.org/10.1016/j.jcrysgro.2014.01.019

[35] Eneman, G. *et al.* Impact of donor concentration, electric field, and temperature effects on the leakage current in germanium p^+n junctions. *IEEE Trans. Electron Devices* **55**, 2287–2296 (2008). https://doi.org/10.1109/TED.2008.927660

[36] Simoen, E. *et al.* On the temperature and field dependence of trap-assisted tunneling current in Ge p^+n junctions. *IEEE Electron Device Lett.* **30**, 562–564 (2009). https://doi.org/10.1109/LED.2009.2017040

[37] Daniels, A. *Field Guide to Infrared Systems, Detectors, and FPAs*. (SPIE Press, 2018).